



ELSEVIER

Contents lists available at ScienceDirect

Electrochimica Acta

journal homepage: [www.elsevier.com/locate/electacta](http://www.elsevier.com/locate/electacta)

## Flexible electrospun iron compounds/carbon fibers: Phase transformation and electrochemical properties



Xiaoli Sheng<sup>a,1</sup>, Tao Li<sup>a,b,1</sup>, Meng Sun<sup>a</sup>, Guiju Liu<sup>a</sup>, Qingye Zhang<sup>a</sup>, Zhibin Ling<sup>a</sup>, Shouwu Gao<sup>c</sup>, Feiyu Diao<sup>b</sup>, Juzheng Zhang<sup>d</sup>, Federico Rosei<sup>e,\*</sup>, Yiqian Wang<sup>a,\*</sup>

<sup>a</sup> College of Physics, Qingdao University, No. 308 Ningxia Road, Qingdao 266071, PR China

<sup>b</sup> College of Textile & Clothing, Qingdao University, No. 308 Ningxia Road, Qingdao 266071, PR China

<sup>c</sup> State Key Laboratory, Qingdao University, No. 308 Ningxia Road, Qingdao 266071, PR China

<sup>d</sup> Shandong Longxing Plastic Film Technology Co., Ltd., Xinhua West Road, Houzhen Industrial Zone, Shouguang, Shandong 262700, PR China

<sup>e</sup> Centre Énergie Matériaux et Télécommunications, Institut National de la Recherche Scientifique, 1650 Boulevard Lionel-Boulet, Varennes, Québec J3X 1S2 Canada

### ARTICLE INFO

#### Article history:

Received 4 December 2021

Revised 7 January 2022

Accepted 10 January 2022

Available online 11 January 2022

#### Keywords:

Flexible electrodes

Iron-compound nanoparticles

Electrospinning

Phase evolution

Electrochemical performance

### ABSTRACT

Flexible electrodes are currently widely studied for applications in energy storage, due to their elasticity and lightweight. Here we describe the fabrication of flexible electrodes obtained by embedding different iron-compound nanoparticles in carbon fibers. The composites are prepared by electrospinning followed by subsequent thermal annealing. We elucidate the phase evolution process of iron compounds in the carbon fibers, i.e.,  $\text{Fe}_3\text{O}_4$ ,  $\text{Fe}_3\text{O}_4/\text{Fe}_3\text{C}$  and  $\text{Fe}_3\text{C}$  being produced in the carbon fibers at 450 °C, 620 °C and 800 °C, respectively. In addition, we investigate the electrochemical performance of  $\text{Fe}_3\text{O}_4$ /carbon fibers ( $\text{Fe}_3\text{O}_4/\text{CF}$ ),  $\text{Fe}_3\text{O}_4/\text{Fe}_3\text{C}$ /carbon fibers ( $\text{Fe}_3\text{O}_4/\text{Fe}_3\text{C}/\text{CF}$ ) and  $\text{Fe}_3\text{C}$ /carbon fibers ( $\text{Fe}_3\text{C}/\text{CF}$ ). When used as anode materials for lithium-ion batteries (LIBs),  $\text{Fe}_3\text{O}_4/\text{CF}$ ,  $\text{Fe}_3\text{O}_4/\text{Fe}_3\text{C}/\text{CF}$  and  $\text{Fe}_3\text{C}/\text{CF}$  electrodes exhibit discharge capacities of 255.3, 478.1 and 169.2  $\text{mAh g}^{-1}$  after 650 cycles at 1  $\text{A g}^{-1}$ , corresponding to 50.2%, 99.3% and 39.3% of the capacities after the second cycle, respectively. Compared with  $\text{Fe}_3\text{O}_4/\text{CF}$  and  $\text{Fe}_3\text{C}/\text{CF}$  electrodes, the  $\text{Fe}_3\text{O}_4/\text{Fe}_3\text{C}/\text{CF}$  electrode delivers higher capacity and better cycling stability. The excellent electrochemical performance of  $\text{Fe}_3\text{O}_4/\text{Fe}_3\text{C}/\text{CF}$  is attributed to the high theoretical specific capacity of  $\text{Fe}_3\text{O}_4$  and the excellent catalytic activity of  $\text{Fe}_3\text{C}$ . Amorphous carbon fibers can buffer large volume changes during the lithium-ion insertion/extraction process. Finally, we evaluate the lithium storage properties of  $\text{Fe}_3\text{O}_4/\text{CF}$  and  $\text{Fe}_3\text{C}/\text{CF}$ . Our work provides insights on the phase evolution and lithium storage mechanisms for iron-compound nanoparticles embedded in carbon fibers.

© 2022 Elsevier Ltd. All rights reserved.

### 1. Introduction

Rechargeable lithium-ion batteries (LIBs) are promising energy storage devices because of their high energy density, low redox potential and long cycle life [1–4]. As a key component of LIBs, anode materials play a decisive role in their electrochemical performance. Over the past decades, graphite has been widely used as anode material for LIBs due to its electrochemical stability. However, graphite exhibits a low theoretical capacity (372  $\text{mAh g}^{-1}$ ) and poor rate performance, which hampers its practical applications [5–7]. Significant efforts have focused on developing new anode materials to overcome these problems, especially nanostruc-

tured metal compounds with a high specific capacity. In addition, most electrodes in LIBs, consisting of active materials such as binders and conductive additives, are heavy and rigid, which limits their electrochemical performance [8]. To overcome the aforementioned problems, it is highly desirable to construct flexible and free-standing materials as realistic alternatives to traditional anode materials.

In recent years, many flexible and freestanding materials have been prepared by various methods such as hydrothermal synthesis [9], electrophoretic deposition [10], and chemical vapor deposition [11]. However, all these processes are tedious and their yields are relatively low. Compared with the above-mentioned preparation methods, electrospinning is more facile, more effective and much cheaper. Through electrospinning, flexible materials can be constructed in the form of one-dimensional (1D) fibers, and easily scaled up for mass production [12]. Moreover, electrospun carbon nanofibers with 1D structures and large surface areas are con-

\* Corresponding authors.

E-mail addresses: [federico.rosei@inrs.ca](mailto:federico.rosei@inrs.ca) (F. Rosei), [yqwang@qdu.edu.cn](mailto:yqwang@qdu.edu.cn) (Y. Wang).

<sup>1</sup> These authors contributed equally to this work.

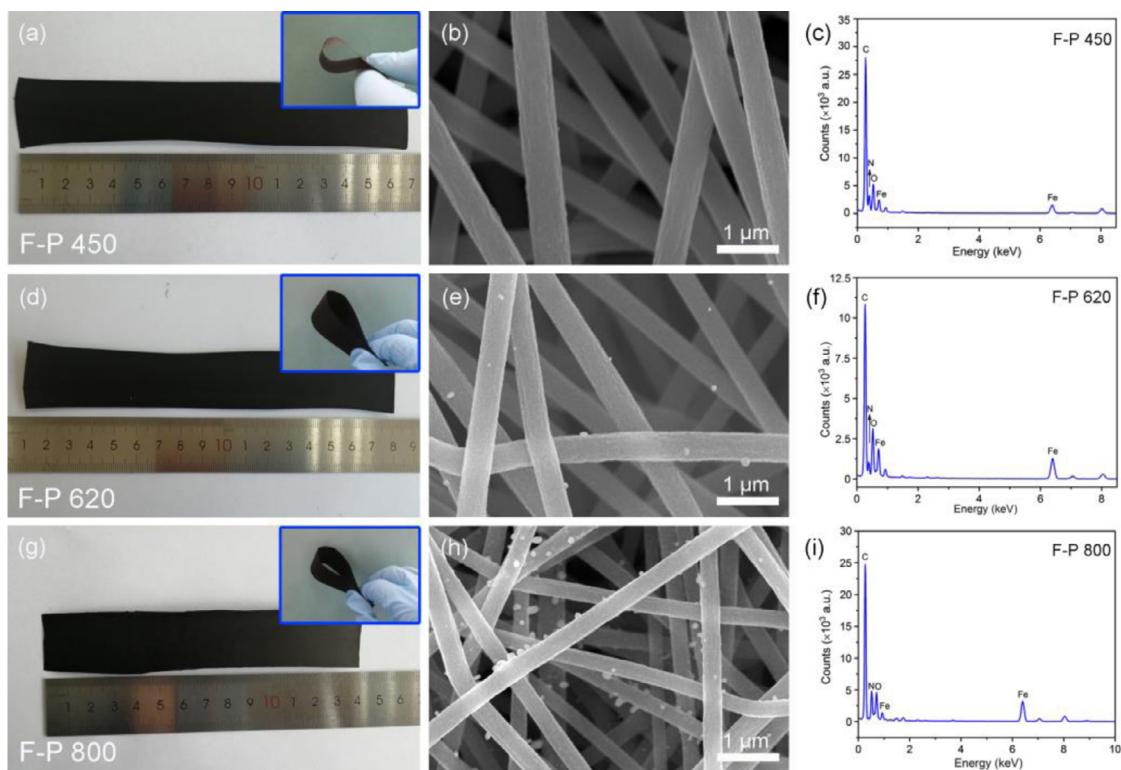


**Fig. 1.** Photographs and SEM images of (a and b) F-P 450, (d and e) F-P 620, (g and h) F-P 800. EDS spectra obtained from (c) F-P 450, (f) F-P 620 and (i) F-P 800.

ductive to electron conductivity and ionic diffusion [13,14]. Compared with pure carbon fibers, the composites of metal compounds embedded in the carbon fibers exhibit better electrochemical performance [15,16]. In such cases, metal compounds can enhance the lithium-ion storage capacity, and the carbon materials can relieve the strain caused by the volume change of the metal compounds during the lithium-ion insertion/extraction process [17].

Among various types of metal compounds, iron compounds have been widely studied because of their variable valence states and excellent electrochemical properties, for example, the high theoretical specific capacity of iron oxides ( $\text{Fe}_2\text{O}_3$  and  $\text{Fe}_3\text{O}_4$ ) and the excellent catalytic activity of iron carbide ( $\text{Fe}_3\text{C}$ ) [18–21]. Thus, many studies focused on fabricating flexible anodes for LIBs by embedding different iron compounds ( $\text{Fe}_2\text{O}_3$ ,  $\text{Fe}_3\text{O}_4$  and  $\text{Fe}_3\text{C}$ ) in the carbon fibers by electrospinning. It was found that the composites of iron compounds/carbon fibers exhibited excellent cycle stability [13] and high specific capacity [22]. In addition,  $\text{Fe}_3\text{O}_4$ /carbon fibers and  $\text{Fe}_3\text{C}$ /carbon fibers demonstrated better flexibility than  $\text{Fe}_2\text{O}_3$ /carbon fibers [21,22]. Although great progress has been achieved in improving the flexibility and electrochemical properties of various iron compounds embedded in carbon fibers, the differences in their lithium storage mechanism are not well understood. In addition, no systematic investigations have been conducted on the phase evolution process of different iron compounds embedded in the carbon fibers. Therefore, it is urgent to clarify the phase evolution process and the lithium storage behaviors of various iron compounds embedded in the carbon fibers, as it can help to further improve their electrochemical properties.

In this work, we prepared  $\text{Fe}_3\text{O}_4$ ,  $\text{Fe}_3\text{O}_4/\text{Fe}_3\text{C}$  and  $\text{Fe}_3\text{C}$  nanoparticles embedded in carbon fibers through electrospinning followed by high-temperature annealing in argon (Ar) atmosphere. We then studied the phase evolution of iron compounds in the carbon fibers. Finally, we investigated the electrochemical performance of different iron-compound nanoparticles/carbon fibers, and explored the differences in the lithium storage behaviors of  $\text{Fe}_3\text{O}_4$  and  $\text{Fe}_3\text{C}$  nanoparticles embedded in the carbon fibers.

## 2. Experimental section

### 2.1. Materials

Polyacrylonitrile (PAN, average Mw 150,000), Iron acetylacetonate [ $\text{Fe}(\text{acac})_3$ , 98%] and N, N-Dimethylformamide (DMF, 99.5%) were commercially purchased from Sinopharm Chemical Reagent Co., Ltd. All chemicals were of analytical grade and directly used as received, without further purification.

### 2.2. Preparation of the nanofibers membrane

PAN (12 wt.%) and  $\text{Fe}(\text{acac})_3$  (8.5 wt.%) were dispersed in DMF and stirred for 2 h to form a viscous mixture. The mixture was then spun into a nanofiber membrane by electrospinning (temperature: 25 °C, humidity: 33~36%, voltage: 20 kV, injection rate: 0.36 mL/h and roll speed: 500–800 rpm). The distance was set as 16 cm from the collecting roll to the syringe needle, and the diameter of the syringe needle pinhole was 0.55 mm. The as-spun nanofiber membrane was dried in air for 2 h to evaporate the organic solvent.

The as-prepared nanofiber membranes were oxidatively stabilized in air at 230 °C for 2 h to attain thermal stability. After stabilization, the nanofiber membranes were annealed at 450, 620 and 800 °C for 2 h at a heating rate of 2 °C/min in Ar flow, respectively. The obtained membranes annealed at 450, 620 and 800 °C were labeled F-P 450, F-P 620 and F-P 800, respectively.

### 2.2. Materials characterization

The morphology of the composites was examined using a field-emission scanning electron microscope (FE-SEM, Sigma 500) operated at 20 kV. Both secondary electron (SE) and backscattered electron (BSE) images were acquired. The chemical compositions were analyzed by X-ray energy-dispersive spectroscopy (EDS, Oxford INCAx-Sight6427) coupled with the SEM system. The elemen-

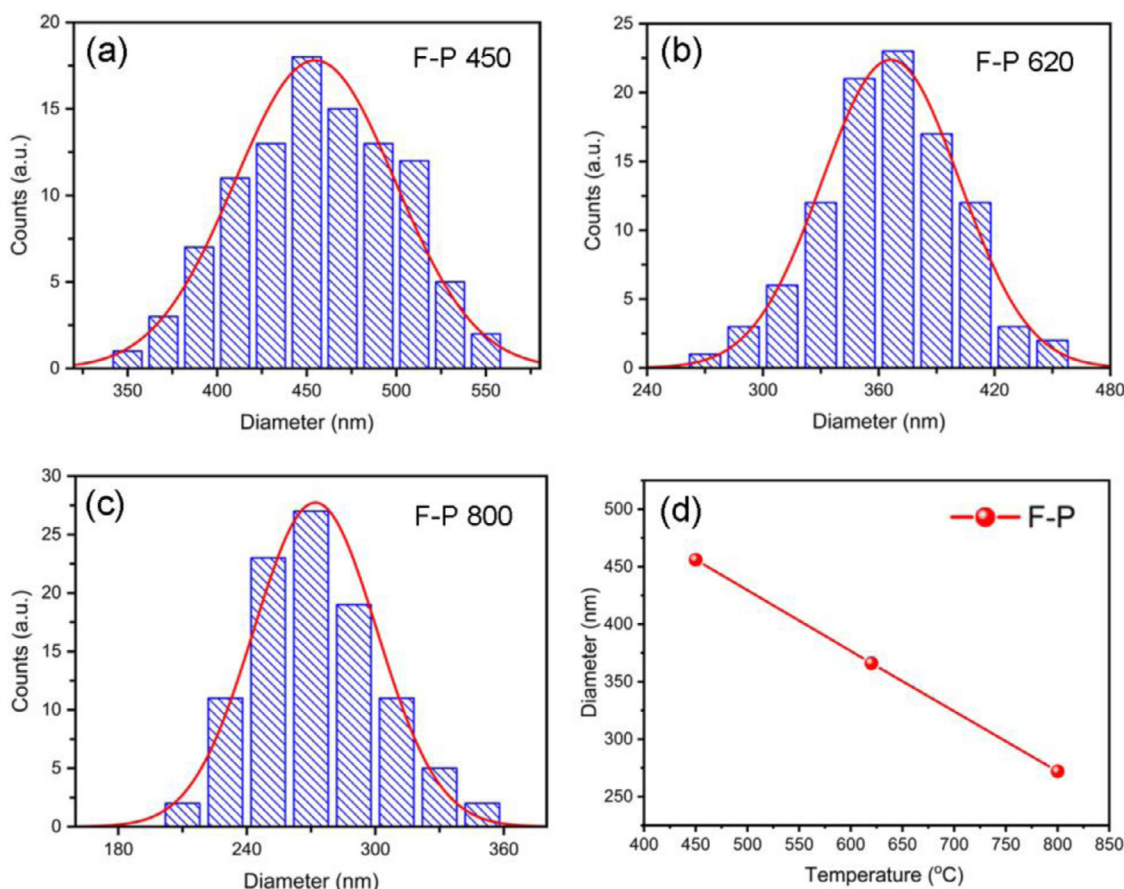


Fig. 2. Diameter distributions of (a) F-P 450, (b) F-P 620 and (c) F-P 800. (d) Plot of average diameter of F-P 450, F-P 620 and F-P 800.

tal mapping of the nanofibers was carried out using an energy-dispersive X-ray spectrometer (EDS, Oxford INCAx-Sight6427).

The crystal structures were analyzed by X-ray diffractometer (XRD, Bruker D8 Advance) with Cu-K $\alpha$  radiation ( $\lambda = 1.5406 \text{ \AA}$ ). X-ray photoelectron spectroscopy (XPS, Thermo Scientific K-Alpha+) data were acquired with an Al K $\alpha$  X-ray source ( $h\nu = 1486.6 \text{ eV}$ ).

Specimens for TEM observations were prepared by grinding the as-prepared membranes, dispersing the powder in ethanol through ultrasonic treatment, dripping several drops onto a holey-carbon-film-supported Cu grid. Bright-field (BF) and high-resolution transmission electron microscopy (HRTEM) images were obtained using a transmission electron microscope (TEM, JEOL JEM 2100F3).

Thermogravimetric analysis (TGA, Germany NETZSCH TG209F3) was carried out at temperatures ranging from 40 to 900 °C with a heating rate of 10 °C/min. The first stage was performed from 40 to 230 °C in air, and the second stage from 230 to 900 °C in Ar atmosphere.

### 2.3. Electrochemical measurements

The flexible membranes of iron-compound nanoparticles/carbon fibers were directly used as binder-free anodes for electrochemical measurements towards lithium-ion storage. The thickness of the composite membranes is  $\sim 200 \mu\text{m}$ , and the mass of the composite anodes is  $\sim 0.0020 \text{ g}$ . The electrolyte was a mixture of 1 M LiPF $_6$  solution and ethylene carbonate (EC)/diethyl carbonate (DEC)/dimethyl carbonate (DMC) (1:1:1 in volume). The CR2025-type coin cells using lithium foil as a counter electrode were assembled in a high-purity Ar-filled glove box, where the moisture and oxygen concentration is less than 0.1 ppm. The cycle and rate

performances were characterized using a LAND CT2001 battery test system in a voltage range from 0.01 to 3.00 V. Cyclic voltammetry (CV) tests were performed on a Metrohm Autolab electrochemical workstation (PGSTAT 302 N) between 0.01 and 3.00 V at different scan rates of 0.1, 0.3, 0.5, 0.8 and 1.0 mV s $^{-1}$ . Electrochemical impedance spectroscopy (EIS) measurements were carried out on a Metrohm Autolab electrochemical workstation (PGSTAT 302 N) under an open-circuit voltage. The EIS tests were carried out at a frequency range from 100 kHz to 0.01 Hz with a disturbance amplitude of 5 mV.

### 3. Results and discussion

Fig. 1a,d and g show photographs of the nanofiber membranes annealed at 450, 620 and 800 °C, and the insets display pictures which show their flexibility. All the membranes can be easily folded without breaking, indicating that they have excellent flexibility. The latter was found to be associated with the oxygen content in the reaction atmosphere. To obtain flexible membranes, it is key to maintain the reaction atmosphere with low or no oxygen because it can react with carbon in PAN during the annealing process and reduce the membranes' flexibility. That is why all the annealing processes are conducted in Ar atmosphere. To study the morphological evolution of nanofibers, we carried out extensive SEM imaging. Fig. 1b,e and h show low-magnification SEM images of F-P 450, F-P 620 and F-P 800, respectively. These images show that fibers are arranged randomly, due to the bending and whipping movement of the electrospinning jet. F-P 450 has a smoother surface than F-P 620 and F-P 800, and the surfaces of F-P 620 and F-P 800 are covered with small particles. This is attributed

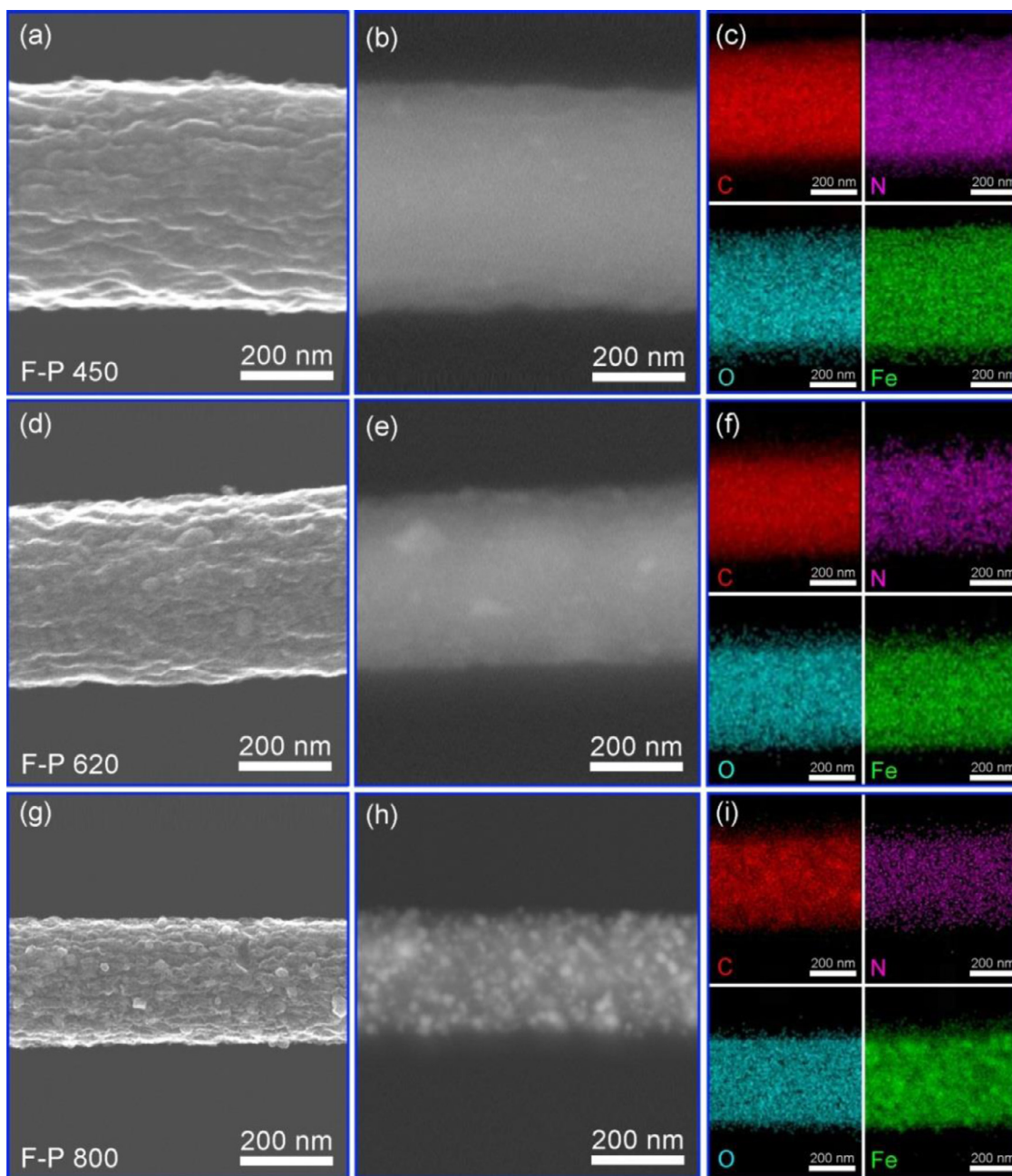


**Fig. 3.** SEM secondary electron and backscattered electron images of (a and b) F-P 450, (d and e) F-P 620 and (g and h) F-P 800. The elemental mapping images related to C, N, O and Fe of (c) F-P 450, (f) F-P 620 and (i) F-P 800.

to the fact that the nanoparticles can more easily diffuse from the inner to the outer surface of the fibers at higher annealing temperatures. With increasing temperatures, the average diameter of the fibers shrinks. The average diameters of F-P 450, F-P 620 and F-P 800 are 456, 366 and 272 nm, respectively (Fig. 2). This is ascribed to the fact that more gases evolve at higher annealing temperatures [23]. EDS measurements were carried out to determine the chemical composition of the F-P 450, F-P 620 and F-P 800. The EDS spectra in Fig. 1c,f and d demonstrate that all the composites consist of C, N, O and Fe elements.

Fig. 3a,d and g show the SEM secondary electron (SE) images of the F-P 450, F-P 620 and F-P 800, respectively. Fig. 3a shows that the surface of the fiber in the F-P 450 exhibits a terrace-like morphology, whereas Fig. 3d shows that a few particles are covered on the outer surface of the fiber in the F-P 620. In contrast, numer-

ous particles are observed discovered on the fiber surface of F-P 800, as shown in Fig. 3g. This suggests that more particles diffuse from the inner to the outer surface with increasing temperature. To show the compositional contrast more clearly, backscattered electron (BSE) imaging was carried out on the fibers fabricated at different annealing temperatures. Fig. 3b,e and h present BSE images of the fibers in the F-P 450, F-P 620 and F-P 800, respectively. A uniform contrast is found in the F-P 450 fiber, while some brighter regions are observed in the fibers of both F-P 620 and F-P 800, which is ascribed to the fact that heavier atoms on the outer surface of the fibers appear brighter in the BSE image.

We then used elemental mapping to further explore the elemental distribution of the fibers. Fig. 3c,f and i show the elemental mapping images of C, N, O and Fe in samples F-P 450, F-P 620 and F-P 800, respectively. Careful observations show that C, N and

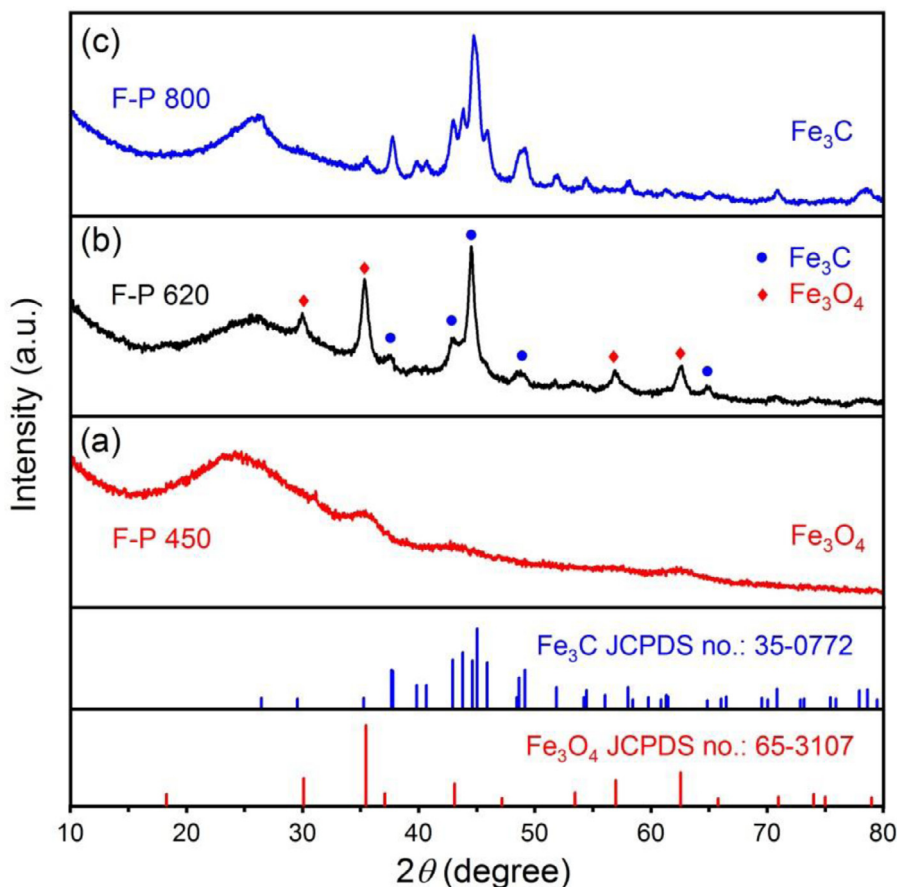


Fig. 4. XRD patterns obtained from (a) F-P 450, (b) F-P 620 and (c) F-P 800.

O are uniformly distributed in individual fibers of F-P 450, F-P 620 and F-P 800. However, the distribution of iron (Fe) is different from that of C, N, and O. The distribution of Fe is uniform in the F-P 450, but uneven in F-P 620 and F-P 800. Based on the above analyses, we conclude that the distribution of Fe becomes less uniform in the fibers produced at higher annealing temperatures.

The crystal structures of F-P 450, F-P 620 and F-P 800 were characterized by XRD, as shown in Fig. 4. A diffusive broad peak at  $\sim 26^\circ$  is found in all the patterns, which corresponds to amorphous carbon. In the XRD pattern of F-P 450 (Fig. 4a), the diffraction peaks at  $35^\circ$ ,  $43^\circ$  and  $62^\circ$  can be well indexed to the (311), (400) and (440) planes of cubic  $\text{Fe}_3\text{O}_4$  (JCPDS no.: 65-3107) [24]. No diffraction peaks from other substances are observed, indicating that the F-P 450 is of high purity. It is observed in Fig. 4b that the diffraction peaks from the F-P 620 are much sharper than those from F-P 450, indicating that the fibers annealed at higher temperatures exhibit better crystallinity. The peak at  $43^\circ$  is attributed to the overlapping of diffraction peaks from (400) plane of cubic  $\text{Fe}_3\text{O}_4$  and (211) and (031) planes of orthorhombic  $\text{Fe}_3\text{C}$  (JCPDS no.: 35-0772) [25]. The obvious peak at  $45^\circ$  originates from the overlap of diffraction peaks from (220) to (031) planes of  $\text{Fe}_3\text{C}$ . This indicates that partial  $\text{Fe}_3\text{O}_4$  converts into  $\text{Fe}_3\text{C}$  by reacting with carbon deriving from PAN at  $620^\circ\text{C}$ . Thus, both  $\text{Fe}_3\text{O}_4$  and  $\text{Fe}_3\text{C}$  co-exist in F-P 620. The quantification analysis of the XRD pattern for F-P 620 shows that the mass ratio of  $\text{Fe}_3\text{O}_4$  and  $\text{Fe}_3\text{C}$  is 1:2. All the diffraction peaks from the F-P 800 (Fig. 4c) are consistent with those of orthorhombic  $\text{Fe}_3\text{C}$ , implying that all  $\text{Fe}_3\text{O}_4$  converts into  $\text{Fe}_3\text{C}$  at  $800^\circ\text{C}$ .

Given the electronegativity of C, N and O ( $\text{O} > \text{N} > \text{C}$ ),  $\text{Fe}(\text{acac})_3$  would react with O, N and C in the PAN in sequence, forming iron oxide ( $\text{Fe}_3\text{O}_4$ ), nitride ( $\text{Fe}_x\text{N}$ ) and carbide ( $\text{Fe}_3\text{C}$ ). However, in our

case, no iron nitride is found in the XRD patterns, which is possibly due to the small amount produced under our experimental conditions. In addition, no  $\text{Fe}_2\text{O}_3$  is found in F-P 450 and F-P 620 because oxygen is inadequate for the formation of  $\text{Fe}_2\text{O}_3$  during the annealing process.

XPS spectra were acquired to analyze the chemical composition of the membranes obtained at different annealing temperatures. Fig. 5a shows the standard spectrum for Fe 2p, and Fig. 5b-d display high-resolution XPS Fe 2p spectra for the F-P 450, F-P 620 and F-P 800, respectively. All the Fe 2p spectra can be fitted using Fe  $2p_{3/2}$  and Fe  $2p_{1/2}$  with different valence states. Fig. 5b displays typical spectra of  $\text{Fe}_3\text{O}_4$  with two diffusive broad peaks located at 710 eV and 724 eV, which are assigned to Fe  $2p_{3/2}$  and Fe  $2p_{1/2}$ , respectively [26,27]. The Fe  $2p_{3/2}$  spectrum can be fitted with two single peaks at 710 eV and 712 eV, corresponding to  $\text{Fe}^{2+}$  (green line) and  $\text{Fe}^{3+}$  (blue line) peaks, respectively. As for the Fe  $2p_{1/2}$  spectrum, the binding energies of the  $\text{Fe}^{2+}$  and  $\text{Fe}^{3+}$  peaks are located at 723 eV and 726 eV [24]. The other peaks near 716, 720, 728 and 733 eV correspond to satellite peaks of Fe 2p [28]. As shown in Fig. 5c, both Fe  $2p_{3/2}$  and Fe  $2p_{1/2}$  spectra can be divided into three peaks. In addition to the typical spectra of  $\text{Fe}_3\text{O}_4$ , two peaks near 707 eV and 722 eV originate from the  $2p_{3/2}$  and  $2p_{1/2}$  of  $\text{Fe}_3\text{C}$  (pink line), respectively [29-32]. This further proves the co-existence of  $\text{Fe}_3\text{O}_4$  and  $\text{Fe}_3\text{C}$  at  $620^\circ\text{C}$ . In Fig. 5d, the binding energies of  $2p_{3/2}$  and  $2p_{1/2}$  (pink line) are 707 and 722 eV, which correspond to  $\text{Fe}_3\text{C}$  at  $800^\circ\text{C}$ . The other peaks near 710, 712, 723 and 726 eV of F-P 800 may originate from the surface oxidation [28].

Extensive TEM examinations were carried out to study the microstructures of F-P 450, F-P 620 and F-P 800 in detail. Fig. 6a,c and e present typical BF TEM images of F-P 450, F-P 620 and F-P

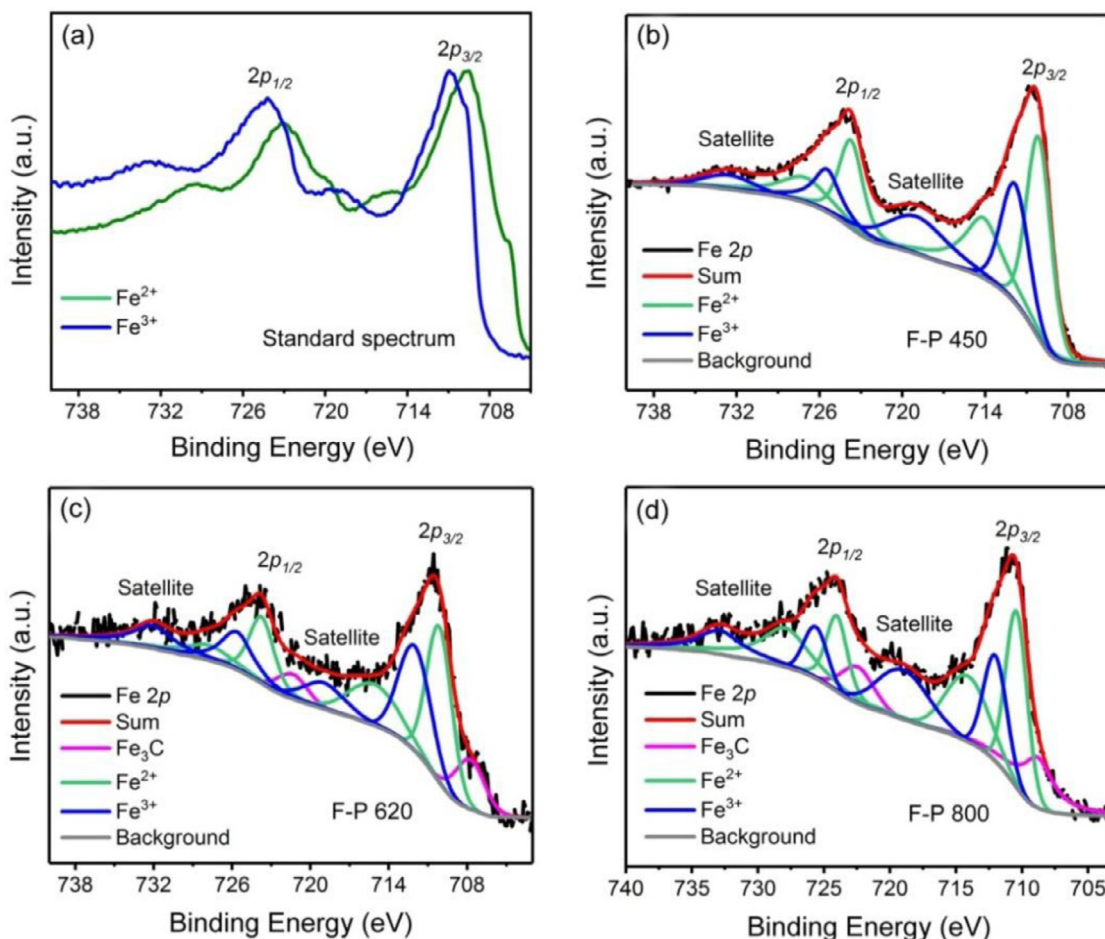


Fig. 5. High-resolution XPS spectra of Fe 2p. (a) standard spectrum, (b) F-P 450, (c) F-P 620 and (d) F-P 800.

800, respectively. No particles are observed on the fiber surface of F-P 450, while many nanoparticles are found on the fiber surface of F-P 620 and F-P 800, consistent with SEM observations. Fig. 6b shows a typical HRTEM image of individual fibers in the F-P 450. The lattice spacing is measured to be 2.55 Å (labeled by yellow lines), which corresponds to the {311} planes of cubic  $\text{Fe}_3\text{O}_4$ . The angle between the two planes is measured to be 85°, which agrees well with its theoretical value. This further proves that the particles formed in F-P 450 are  $\text{Fe}_3\text{O}_4$ . Fig. 6d shows a typical HRTEM image of the fiber in sample F-P 620, which consists of two different kinds of nanoparticles labeled by yellow and green lines, respectively. In the particle labeled by yellow lines, the lattice spacing is measured to be 2.55 Å, corresponding to the {311} planes of  $\text{Fe}_3\text{O}_4$ . The angle between the two planes is measured to be 83°, slightly different from its theoretical value of 85°, which is ascribed to the fact that the nanoparticle is under stress and its orientation deviates a little from the [112] zone-axis. In the particle labeled by green lines, the interplanar spacings of 2.03 Å and 2.40 Å can be indexed to the (031) and (210) planes of orthorhombic  $\text{Fe}_3\text{C}$ , respectively. The angle between the two planes is measured to be 72°, consistent with its theoretical value. This confirms that  $\text{Fe}_3\text{O}_4$  and  $\text{Fe}_3\text{C}$  co-exist in F-P 620. The typical HRTEM image of F-P 800 in Fig. 6f displays clear lattices with lattice spacings of 2.24 Å and 2.09 Å (labeled by green lines). The two planes correspond to the (201) and (102) planes of orthorhombic  $\text{Fe}_3\text{C}$ , respectively. The angle between the two planes is measured to be 85°, consistent with its theoretical value. Therefore, we conclude that cubic  $\text{Fe}_3\text{O}_4$  completely transforms into orthorhombic  $\text{Fe}_3\text{C}$  at 800 °C.

TGA measurements were carried out to further determine the decomposition temperature for  $\text{Fe}(\text{acac})_3$ -PAN fibers (F-P). Fig. 7a shows the TGA curves of F-P and PAN fibers (P). The F-P and P curves are obtained by simulating the preparation process of iron compounds/carbon fibers. It is challenging to determine, from the TGA curves, the temperature range in which the phase transformation of different iron compounds takes place during the annealing process of F. To demonstrate the phase evolution process of iron compounds embedded in the carbon fibers more clearly, the TGA curve of F in the F-P fibers (Fig. 7b) is obtained using the following equation.

$$\begin{aligned} W_F &= 100\% - [(100\% - W_{F-P}) - (100\% - W_P)] \\ &= 100\% - (W_P - W_{F-P}) \end{aligned} \quad (1)$$

Fig. 7b shows that there are four obvious plateaus and two evident declines in the TGA curve of F. The plateau means that a stable phase forms at a certain temperature range, while the decline reflects that a phase transformation occurs at a certain temperature range. F remains stable until the temperature reaches 150 °C. A rapid weight loss of F is found from 150 to 230 °C due to its significant decomposition in air. From 230 to 310 °C, the weight of F barely changes since the decomposition of F is extremely slow in Ar atmosphere. From 310 to 603 °C, the weight of F starts to increase and then remains unchanged, which is attributed to the formation of  $\text{Fe}_3\text{O}_4$ . From 603 to 730 °C, the weight loss of F is above 8%, which is consistent with the phase transformation from  $\text{Fe}_3\text{O}_4$  to  $\text{Fe}_3\text{C}$ . No weight loss of F is observed beyond 730 °C, indicating

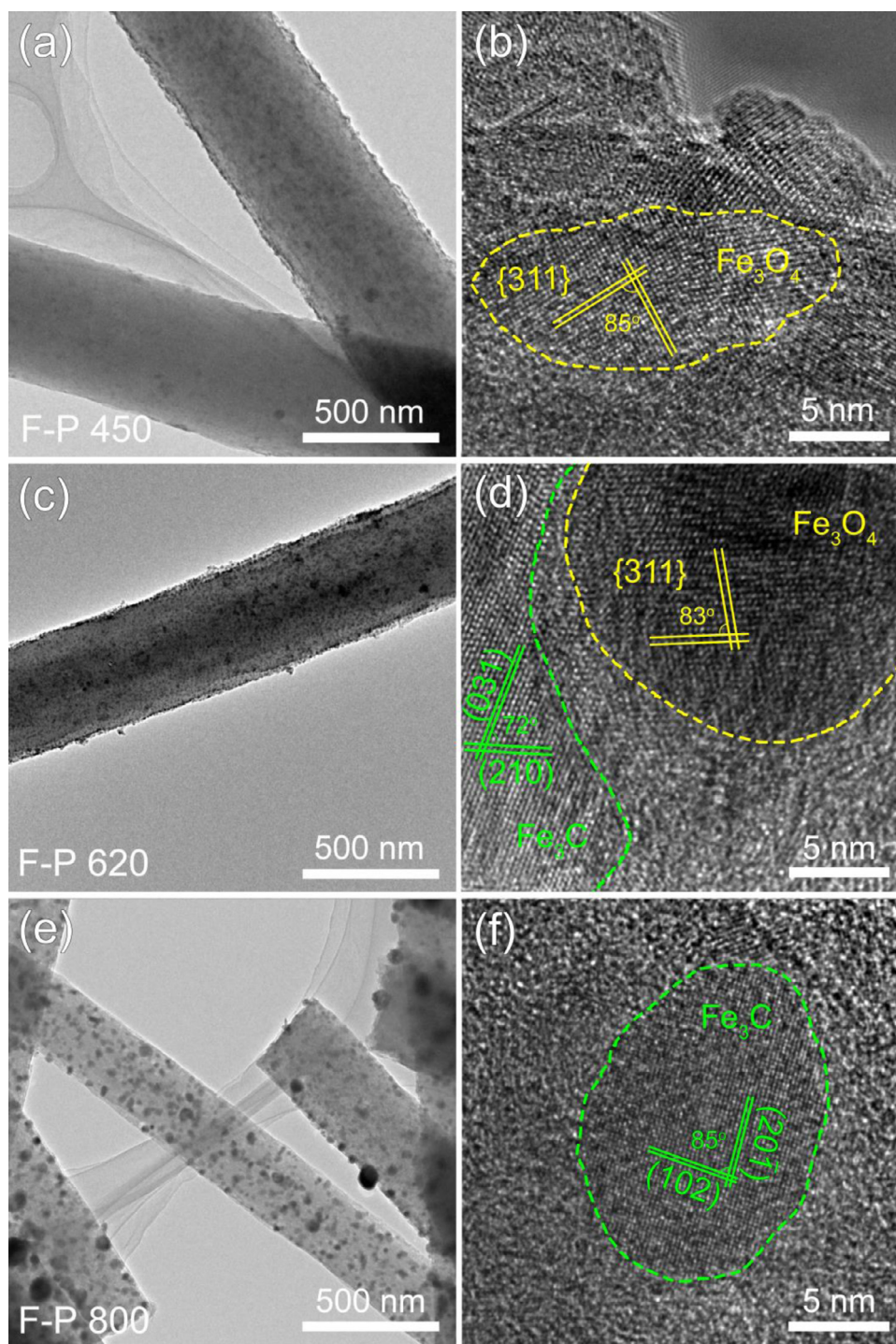
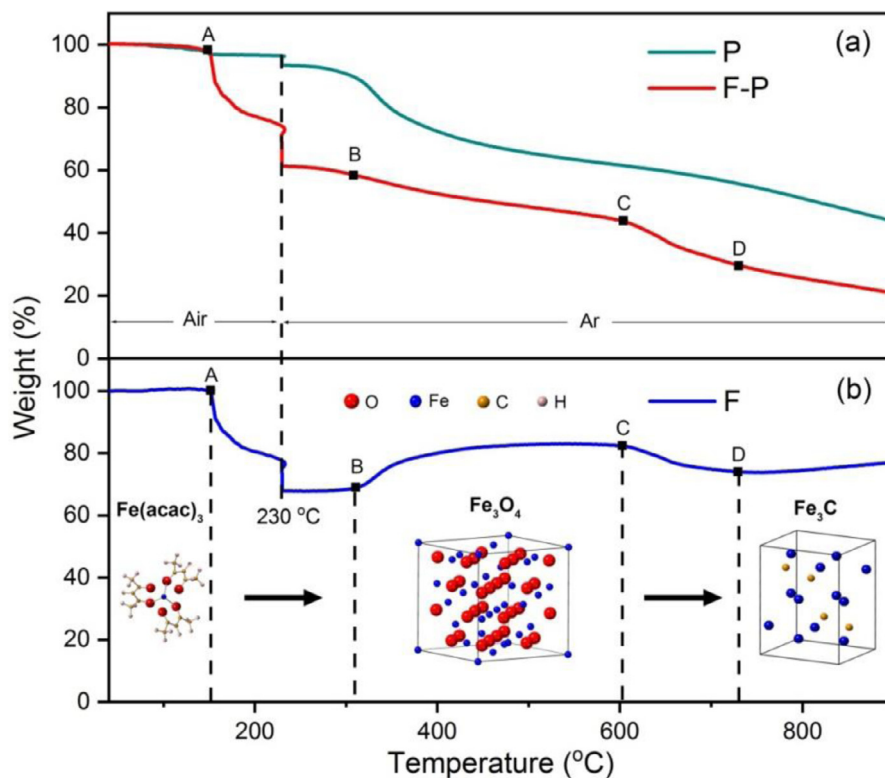


Fig. 6. Typical BF TEM and HRTEM images of (a and b) F-P 450, (c and d) F-P 620 and (e and f) F-P 800.

that F transforms into another stable phase, which is confirmed to be  $\text{Fe}_3\text{C}$  from the above XRD and TEM analyses.

To evaluate the electrochemical properties, F-P 450, F-P 620 and F-P 800 were tested as anode materials for LIBs. Fig. 8a shows the CV curves of F-P 450 electrode in the 0.01–3.00 V voltage range at a scan rate of  $0.3 \text{ mV s}^{-1}$ . During the initial cathodic process, a distinct reduction peak at 0.6 V is observed, which is attributed to the formation of the solid electrolyte interphase (SEI) film and the lithiation reaction of  $\text{Fe}_3\text{O}_4$  to form Fe and  $\text{Li}_2\text{O}$ . In the subsequent cycle, the reduction peak shifts to 0.7 V due to the irreversibility of the SEI film [13]. During the anodic process, an oxidation peak

shifts from 1.1 to 1.6 V, corresponding to the delithiation reactions obtained by oxidizing Fe to  $\text{Fe}^{2+}$  and  $\text{Fe}^{3+}$  [13]. Fig. 8b displays typical CV curves of F-P 620 electrode at a scan rate of  $0.3 \text{ mV s}^{-1}$ . In the first cathodic process, a reduction peak at 0.5 V is ascribed to the formation of the SEI film [21]. In the subsequent cycle, this peak disappears due to the occurrence of some irreversible reactions (e.g. the formed irreversible SEI film and the possible polarization of the active materials) [21]. The subtle cathodic peak at 0.8 V and the weak anodic peak at 1.2 V mainly correspond to the redox reaction of iron compound [33]. Fig. 8c presents typical CV curves of the F-P 800 electrode in the 0.01–3.00 V voltage range



**Fig. 7.** (a) TGA curves of Fe(acac)<sub>3</sub>-PAN fibers (F-P) and PAN fibers (P). (b) The calculated TGA curve of Fe(acac)<sub>3</sub> (F) in the Fe(acac)<sub>3</sub>-PAN fibers. The insets display various iron compounds produced at different temperature stages.

at a scan rate of 0.3 mV s<sup>-1</sup>. During the initial cathodic process, a reduction peak at 0.5 V is found, which is associated with the lithiation process and the formed SEI film [21]. The two oxidation peaks at 1.6 and 1.9 V originate from the reversible oxidation of Fe [34]. Fig. 8d shows the first cycle discharge/charge profiles of the three electrodes at 1 A g<sup>-1</sup>. The initial discharge capacities are 1031.9, 858.7 and 747.6 mAh g<sup>-1</sup> for the F-P 450, F-P 620 and F-P 800 electrodes, respectively. The gradual decline of the initial discharge capacities for the F-P 450, F-P 620 and F-P 800 electrodes is attributed to the decreasing content of Fe<sub>3</sub>O<sub>4</sub> in the electrodes, which possesses a high theoretical specific capacity of 925 mAh g<sup>-1</sup> [13].

Fig. 9a illustrates the rate capability of the three electrodes at different current densities. Compared with the F-P 450 and F-P 800 electrodes, the F-P 620 electrode exhibits better rate capability with an average discharge capacity of 539.3, 489.4, 447.5, 403.3 and 358.0 mAh g<sup>-1</sup> at 0.1, 0.2, 0.5, 1 and 2 A g<sup>-1</sup>, respectively. When the current density returns to 0.1 A g<sup>-1</sup>, the discharge capacity of the F-P 620 electrode remains at 630 mAh g<sup>-1</sup> after 150 cycles. To investigate their cycling performance, the three electrodes were tested for 650 cycles at a high current density of 1 A g<sup>-1</sup> (Fig. 9b). The F-P 450 and F-P 800 electrodes exhibit discharge capacities of 255.3 and 169.2 mAh g<sup>-1</sup> after 650 cycles at 1 A g<sup>-1</sup>, respectively. At the high current density of 1 A g<sup>-1</sup>, the structure of Fe<sub>3</sub>C can be destructed, leading to the poor cycling performance. By contrast, the discharge capacity of the F-P 620 electrode increases to 612.3 mAh g<sup>-1</sup> after 325 cycles at 1 A g<sup>-1</sup>, and then retains 478.1 mAh g<sup>-1</sup> after 650 cycles. In the initial 325 cycles, the enhanced capacity may be attributed to the catalytic activation of Fe<sub>3</sub>C. Fe<sub>3</sub>C, as a catalyst, can gradually reduce the concentration of SEI components and promote the reversible formation/decomposition of the SEI film during cycling, resulting in the increase of reversible capacity [35]. The discharge capacities of the F-P 450, F-P 620 and F-P 800 electrodes after 650 cycles at 1 A g<sup>-1</sup>

correspond to 50.2%, 99.3% and 39.3% of the capacities after the second cycle, respectively. This indicates that the F-P 620 shows much better cycling stability than the F-P 450 and F-P 800 at a high current density of 1 A g<sup>-1</sup>. Compared with the F-P 620 before cycle (Fig. 1), its morphology exhibits no obvious changes after 650 cycles at 1 A g<sup>-1</sup> (Fig. 10), demonstrating that the F-P 620 electrode has good stability. The good stability is attributed to the following reasons: (i) The amorphous carbon can relieve strain caused by the volume change of the Fe<sub>3</sub>O<sub>4</sub> and Fe<sub>3</sub>C in the process of Li<sup>+</sup> insertion/extraction. (ii) Fe<sub>3</sub>C possesses excellent catalytic activity, which promotes the partially reversible formation/decomposition of the SEI film [36]. The electrochemical performances of the iron-based anode materials in the previous literature are summarized in Table 1. It can be seen that the Fe<sub>3</sub>O<sub>4</sub>/Fe<sub>3</sub>C/CF anode exhibits better electrochemical performances (612.3 mAh g<sup>-1</sup> after 325 cycles, 478.1 mAh g<sup>-1</sup> after 650 cycles) than Fe<sub>3</sub>O<sub>4</sub>, Fe/Fe<sub>3</sub>C or Fe<sub>3</sub>C composited with carbon materials, and shows a comparable electrochemical performance of other Fe<sub>3</sub>O<sub>4</sub>/Fe<sub>3</sub>C composited carbon anode materials. Thus, the Fe<sub>3</sub>O<sub>4</sub>/Fe<sub>3</sub>C/CF could be a promising anode material for LIBs.

To obtain insights into the Li-storage mechanism of the Fe<sub>3</sub>O<sub>4</sub>/CF electrode, a series of CV measurements at different scan rates were performed. As presented in Fig. 11a, the profiles of the CV curves remain unchanged at various scan rates, indicating that similar electrochemical reactions take place. The current (*i*) and scan rate (*v*) usually abides by a power-law relationship as follows [32].

$$i = av^b, \quad (2)$$

where *a* and *b* are constants. The value of *b* is determined by the slope of the log(*i*) vs. log(*v*) [39]. When *b* is close to 0.5, the lithium storage is dominated by a diffusion-controlled process; when *b* approaches to 1.0, the lithium storage is mainly governed by a pseudocapacitive process. The log(*i*)-log(*v*) plots are depicted

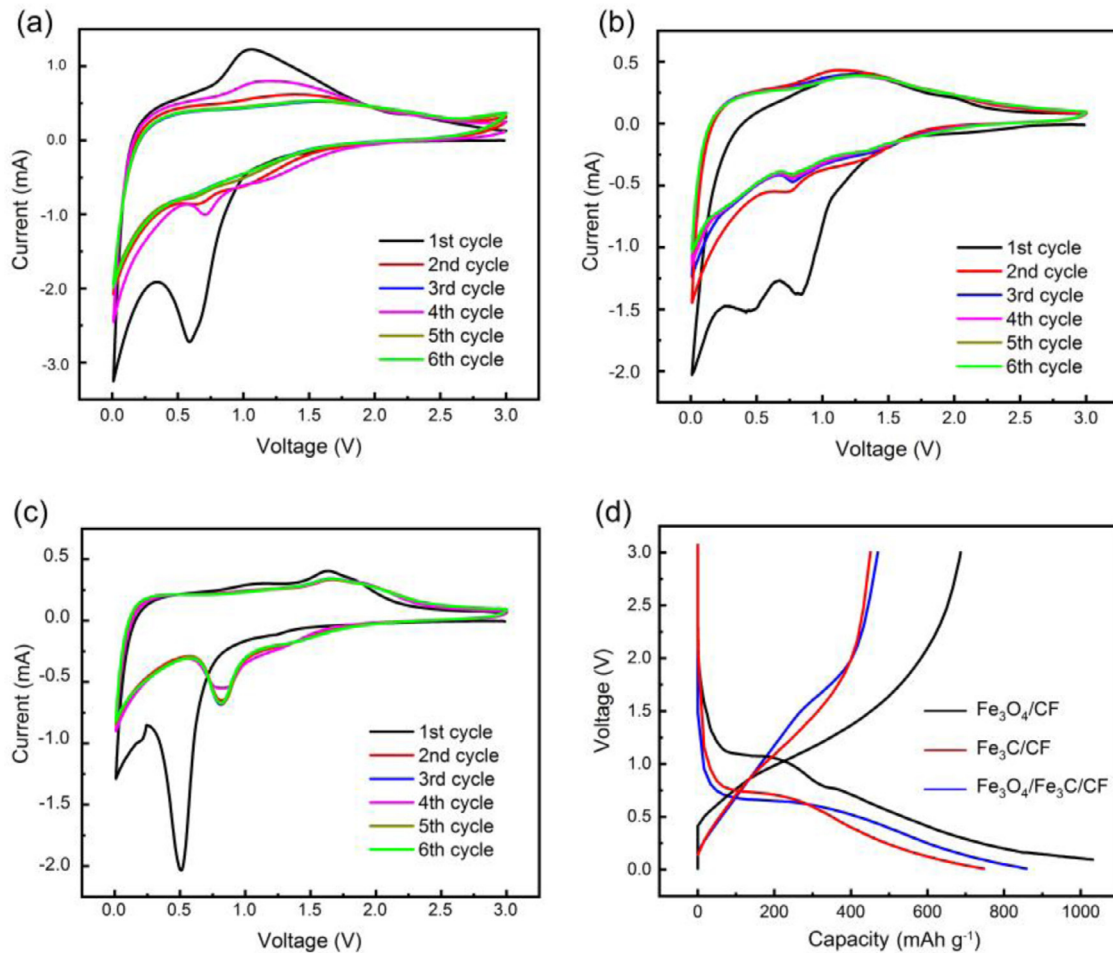


**Fig. 8.** CV curves of (a) F-P 450, (b) F-P 620 and (c) F-P 800 electrodes at a scan rate of 0.3 mV s<sup>-1</sup>. (d) Initial voltage versus capacity curves of F-P 450, F-P 620 and F-P 800 electrodes at a current density of 1 A g<sup>-1</sup>.

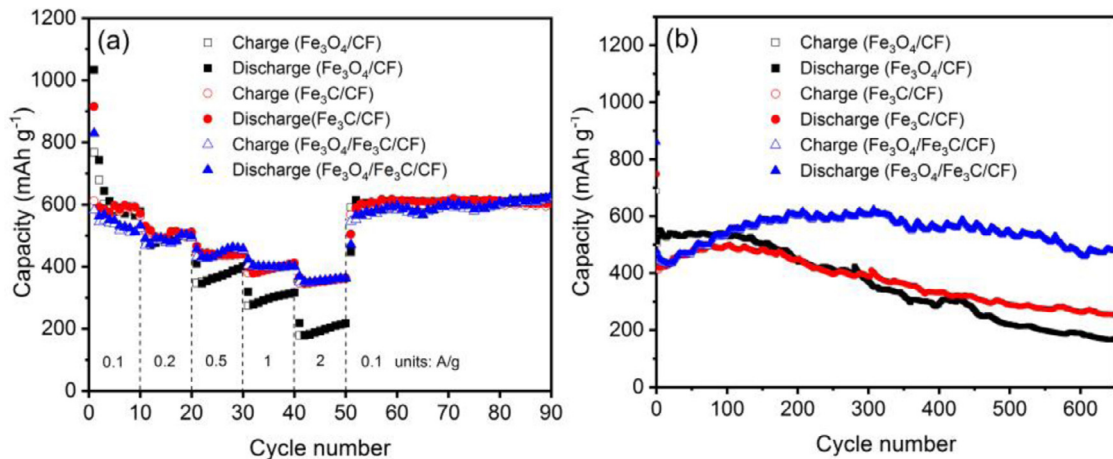


**Fig. 9.** (a) Rate performance of F-P 450, F-P 620 and F-P 800 electrodes at different current densities. (b) Cycling performance of F-P 450, F-P 620 and F-P 800 electrodes at a current density of 1 A g<sup>-1</sup>.

in Fig. 11b. The  $b$  values for both cathodic (0.69) and anodic (0.59) peaks are close to 0.5, indicating that the lithium storage mechanism of Fe<sub>3</sub>O<sub>4</sub>/CF electrode is dominated by a diffusion-controlled process. To be more precise, the contribution ratio of diffusion-controlled and pseudocapacitive processes at different scan rates can be estimated using the following equation [32].

$$i = k_1 v + k_2 v^{1/2}, \quad (3)$$

where  $k_1 v$  and  $k_2 v^{1/2}$  represent the pseudocapacitive and diffusion-controlled contributions, respectively. For example, the pseudocapacitive contribution at a scan rate of 0.3 mV s<sup>-1</sup> is demonstrated by a blue region in Fig. 11c. The contribution ratios of the diffusion-controlled and pseudocapacitive processes at different scan rates are summarized in Fig. 11d for the Fe<sub>3</sub>O<sub>4</sub>/CF electrode. The pseudocapacitive contribution (blue region) is quantified as 31,35,40,43 and 46% at a scan rate of 0.1,0.3,0.5,0.8 and

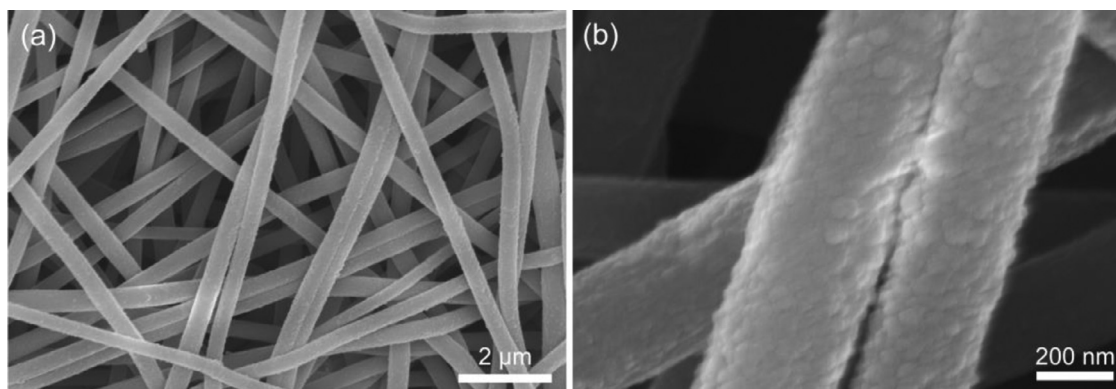


Fig. 10. SEM images of the F-P 620 electrode after 650 cycles at a current density of  $1 \text{ A g}^{-1}$ .

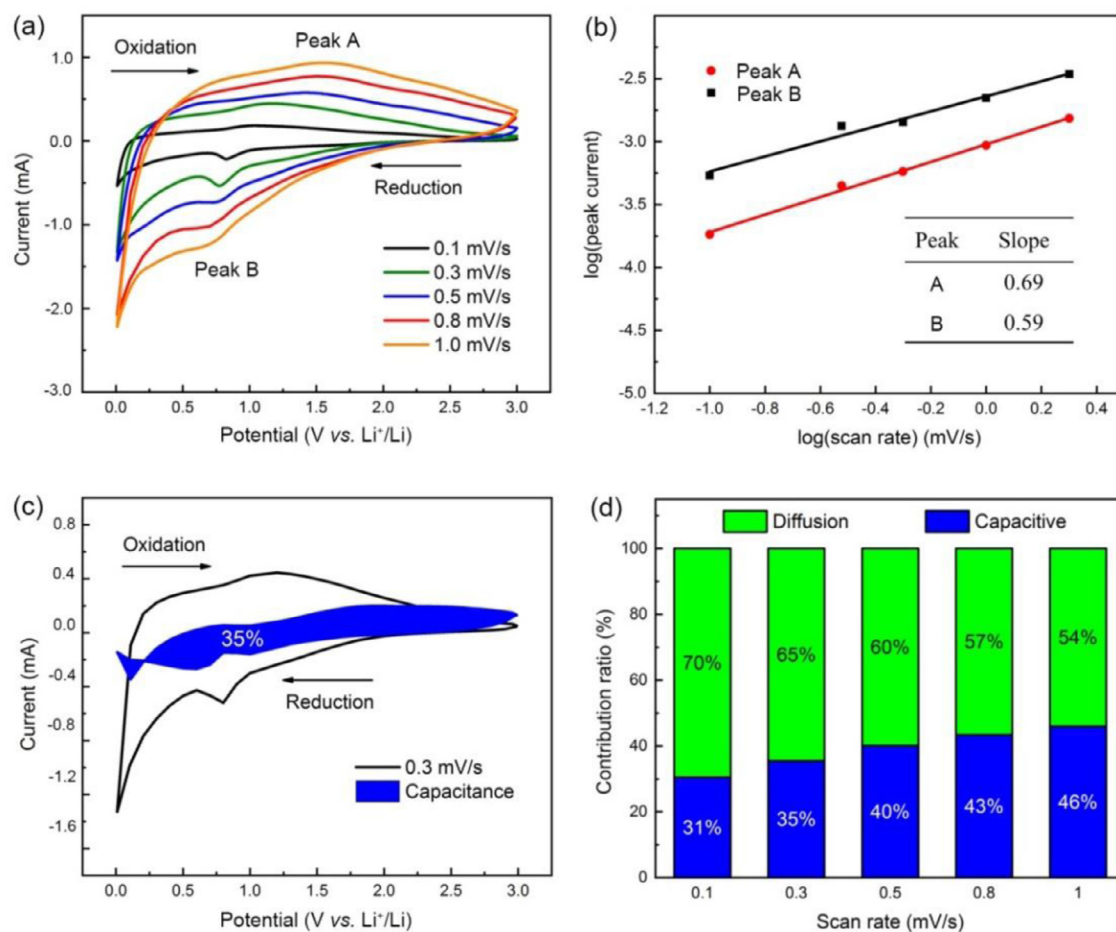


Fig. 11. (a) CV curves of the  $\text{Fe}_3\text{O}_4/\text{CF}$  electrode at various scan rates. (b) Values of  $b$  (slope) at different peak currents after linear fitting. (c) Contribution ratio of capacitance at a scan rate of  $0.3 \text{ mV s}^{-1}$ . (d) Diffusion-controlled contribution (green region) and capacitive contribution (blue region) at different scan rates for the  $\text{Fe}_3\text{O}_4/\text{CF}$  electrode.

$1.0 \text{ mV s}^{-1}$ , which indicates that the lithium storage behavior of  $\text{Fe}_3\text{O}_4/\text{CF}$  electrode is dominated by a diffusion-controlled process at scan rates from  $0.1$  to  $1.0 \text{ mV s}^{-1}$ .

For the  $\text{Fe}_3\text{C}/\text{CF}$  electrode, its lithium storage behavior was explored through a series of CV measurements at different scan rates. In Fig. 12a, the CV curves display similar profiles at different scan rates from  $0.1$  to  $1.0 \text{ mV s}^{-1}$ . Fig. 12b shows the  $\log(i)-\log(v)$  plots of  $\text{Fe}_3\text{C}/\text{CF}$  electrode. The  $b$  values for cathodic and anodic peaks are calculated to be  $0.85$  and  $0.90$ , respectively, which is close to  $1.0$ . This means that the lithium-ion storage mechanism of the  $\text{Fe}_3\text{C}/\text{CF}$  electrode is mainly governed by a pseudocapaci-

tive process. Fig. 12c shows that  $81\%$  of the lithium-ion storage in the electrode is calculated as pseudocapacitance (blue region) at a scan rate of  $0.3 \text{ mV s}^{-1}$ . Fig. 12d illustrates contribution ratios of diffusion-controlled and pseudocapacitive processes at different scan rates. It clearly shows that the capacity of  $\text{Fe}_3\text{C}/\text{CF}$  electrode is dominated by a pseudocapacitive process from  $0.1$  to  $1.0 \text{ mV s}^{-1}$ .

EIS measurements were carried out to further explore the electrochemical reaction kinetics of the F-P 450, F-P 620 and F-P 800 electrodes. Fig. 13a presents EIS spectra obtained from the F-P 450, F-P 620 and F-P 800 electrodes. All the EIS spectra consist of a semicircle in the high-frequency region and an inclined line

**Table 1**  
A comparison of the electrochemical properties of the iron-based anode materials for LIBs.

Anode materials	Cycling performance			Rate capability		Refs.
	Current density (A g <sup>-1</sup> )	Cycle number	Capacity (mAh g <sup>-1</sup> )	Current density (A g <sup>-1</sup> )	Capacity (mAh g <sup>-1</sup> )	
Fe <sub>3</sub> O <sub>4</sub> /Fe <sub>3</sub> C/Fe@C composite	1.0	500	470	0.4 1.0	403 470	[25]
Porous carbon spheres doped with Fe <sub>3</sub> C	1.0	100	400	0.2 2.0	423 221	[33]
Yolk-shell Fe <sub>3</sub> O <sub>4</sub> @C anodes with Fe <sub>3</sub> C	1.0	300	~600	0.2 2.0	~700 ~450	[36]
Fe <sub>3</sub> O <sub>4</sub> /C/rGO composite	0.2	500	333	0.02 0.2	932 333	[37]
Graphitic carbon encapsulated Fe/Fe <sub>3</sub> C	0.5	500	154	0.1 5.0	<400 <100	[38]
Fe <sub>3</sub> O <sub>4</sub> /Fe <sub>3</sub> C/CF	1.0	650	478	0.1 2.0	540 358	This work

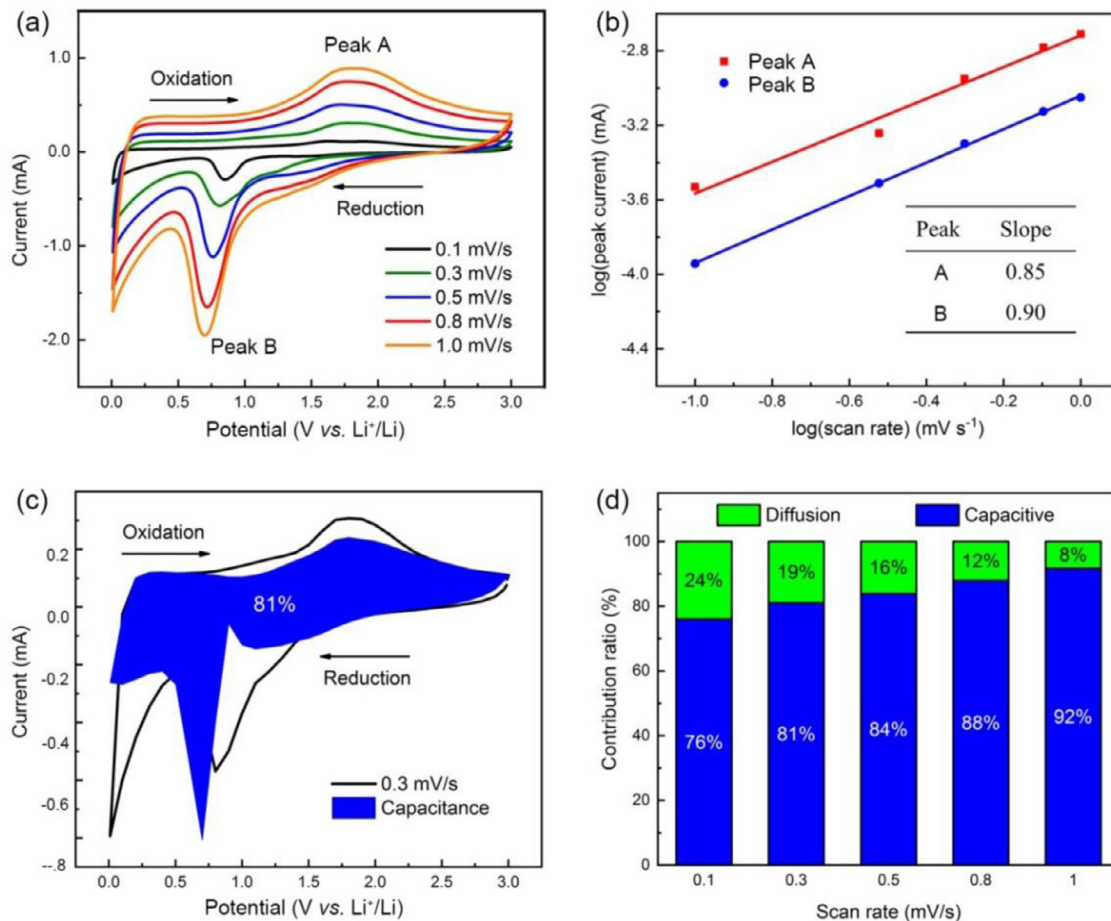


**Fig. 12.** (a) CV curves of the Fe<sub>3</sub>C/CF electrode at various scan rates. (b) Values of  $b$  (slope) at different peak currents after linear fitting. (c) Contribution ratio of capacitance at a scan rate of 0.3 mV s<sup>-1</sup>. (d) Diffusion-controlled contribution (green region) and capacitive contribution (blue region) at different scan rates for the Fe<sub>3</sub>C/CF electrode.

in the low-frequency region, which can be fitted with an equivalent circuit model as shown in the inset of Fig. 13a.  $R_s$ ,  $R_{ct}$ ,  $W$  and CPE represent the electrolyte resistance, charge-transfer resistance, Warburg impedance and double-layer capacitance, respectively [13]. The  $R_{ct}$  values are 424, 110 and 92  $\Omega$  for the F-P 450, F-P 620 and F-P 800 electrodes, respectively. The semicircle diameters of F-P 450, F-P 620 and F-P 800 gradually decrease in the high-frequency region, indicating that the electrodes obtained at higher annealing temperatures possess a lower charge-transfer impedance. In addition, the inclined line in the low-frequency region is related to the lithium-ion diffusion of the electrode. The lithium-ion diffusion coefficient ( $D_{Li}$ ) can be calculated using the

following equations [40,41].

$$D_{Li} = \frac{R^2 T^2}{2A^2 n^4 F^4 C^2 \sigma^2}, \quad (4)$$

$$Z' = R_s + R_{ct} + \sigma \omega^{-0.5}, \quad (5)$$

where the constant values of  $F$  and  $R$  are the Faraday constant (96,485 C mol<sup>-1</sup>) and gas constant (8.314 J K<sup>-1</sup> mol<sup>-1</sup>), respectively.  $A$  is the electrode area ( $1.54 \times 10^{-4}$  m<sup>2</sup>),  $n$  is the number of transferred electrons during conversion of per single molecule (i.e., Fe<sub>3</sub>O<sub>4</sub>,  $n = 8$ ; Fe<sub>3</sub>C,  $n = 1/6$ ),  $T$  is 298.17 K and  $C$  represents the lithium-ion concentration of the electrode. Fig. 13b shows the

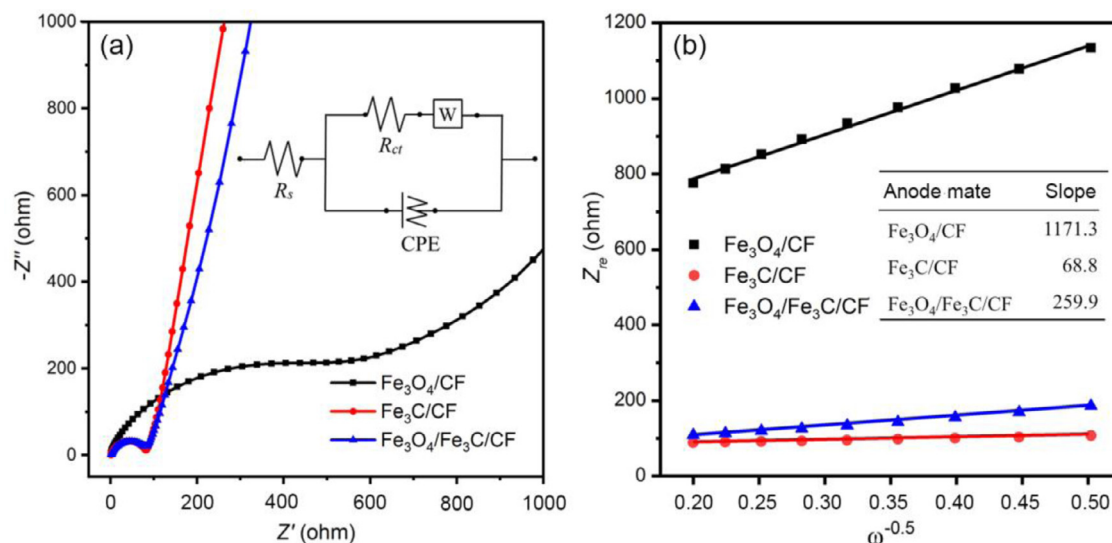


**Fig. 13.** (a) EIS spectra of the F-P 450, F-P 620 and F-P 800 electrodes. The inset shows the equivalent circuit used for fitting impedance spectra. (b) Graph of  $Z_{re}$  plotted against  $\omega^{-0.5}$ .

graph of  $Z_{re}$  plotted against  $\omega^{-0.5}$ . The  $\sigma$  values of the F-P 450, F-P 620 and F-P 800 electrodes are determined to be 1171.3, 259.9 and 68.8  $\Omega \text{ s}^{-0.5}$ , respectively. The  $D_{Li}$  is calculated to be  $5.26 \times 10^{-27}$ ,  $1.52 \times 10^{-24}$  and  $9.05 \times 10^{-19} \text{ cm}^2 \text{ s}^{-1}$  for the F-P 450, F-P 620 and F-P 800 electrodes, respectively. The  $D_{Li}$  of F-P 450, F-P 620 and F-P 800 electrodes gradually increase, which is associated with the diffusion length of lithium ions [42] and the pseudocapacitive behavior [43]. On the one hand, the diameter of fibers shrinks with increasing annealing temperatures, which results in a short diffusion length for the lithium ions. On the other hand, the content of Fe<sub>3</sub>C substantially rises with increasing annealing temperatures, which yields the higher contribution of pseudocapacitance. The higher pseudocapacitance contribution of the electrode can provide more rapid kinetics for Li<sup>+</sup> insertion/extraction [43]. The EIS results imply that the electrode materials fabricated at higher annealing temperature exhibit a lower charge-transfer impedance and higher  $D_{Li}$ .

#### 4. Conclusions and perspectives

In summary, Fe<sub>3</sub>O<sub>4</sub>/CF, Fe<sub>3</sub>O<sub>4</sub>/Fe<sub>3</sub>C/CF and Fe<sub>3</sub>C/CF were prepared by electrospinning followed by an annealing at 450, 620 and 800 °C, respectively. Compared with the Fe<sub>3</sub>O<sub>4</sub>/CF and Fe<sub>3</sub>C/CF electrodes, Fe<sub>3</sub>O<sub>4</sub>/Fe<sub>3</sub>C/CF electrode delivers better electrochemical performance. The initial discharge capacity of Fe<sub>3</sub>O<sub>4</sub>/Fe<sub>3</sub>C/CF is 747.6 mAh g<sup>-1</sup> at 1 A g<sup>-1</sup>, which maintains 478.1 mAh g<sup>-1</sup> after 650 cycles, corresponding to 99.3% of the capacity after the second cycle. The excellent electrochemical performance is attributed to the flexible composite fibers, which can relieve strain caused by the volume change of the Fe<sub>3</sub>O<sub>4</sub> and Fe<sub>3</sub>C in the process of Li<sup>+</sup> insertion/extraction. The lithium storage behavior of the Fe<sub>3</sub>O<sub>4</sub>/CF electrode is dominated by a diffusion-controlled process, while the lithium storage mechanism of the Fe<sub>3</sub>C/CF electrode is mainly governed by a pseudocapacitive process. This work can deepen the understanding of the phase evolution and lithium storage mechanisms for the iron compounds embedded in the carbon fibers.

#### Declaration of Competing Interest

There are no conflicts to declare.

#### Credit authorship contribution statement

**Xiaoli Sheng:** Investigation, Formal analysis, Writing – original draft. **Tao Li:** Conceptualization, Investigation, Writing – original draft, Writing – review & editing. **Meng Sun:** Formal analysis, Writing – review & editing. **Guiju Liu:** Formal analysis, Methodology. **Qingye Zhang:** Formal analysis, Validation. **Zhibin Ling:** Formal analysis, Validation. **Shouwu Gao:** Resources. **Feiyu Diao:** Formal analysis, Methodology. **Juzheng Zhang:** Resources. **Federico Rosei:** Supervision, Writing – review & editing. **Yiqian Wang:** Conceptualization, Funding acquisition, Supervision, Writing – review & editing.

#### Acknowledgments

The authors would like to thank the financial support from High-end Foreign Experts Recruitment Programs (Grant Nos.: GDW20173500154, GDW20163500110), Shandong Province “Double-Hundred Talent Plan” (Grant No.: WST2018006), Shandong Province High-end Foreign Experts Recruitment Program, and the Top-notch Innovative Talent Program of Qingdao City, China (Grant no.: 13-CX-8). Y. Q. Wang would also like to thank the financial support from the Taishan Scholar Program of Shandong Province, China, Qingdao International Center of Semiconductor Photoelectric Nanomaterials, and Shandong Provincial University Key Laboratory of Optoelectrical Material Physics and Devices. F.R. acknowledges the Canada Research Chairs program for partial salary support.

#### References

- [1] X.C. Li, Z. Chu, H.L. Jiang, Y. Dai, W.J. Zheng, A. Liu, X.B. Jiang, G.H. He, Redistributing Li-ion flux and homogenizing Li-metal growth by N-doped hierarchically porous membranes for dendrite-free lithium metal batteries, *Energy Storage Mater.* 37 (2021) 233–242.
- [2] J.M. Zheng, M.H. Engelhard, D.H. Mei, S.H. Jiao, B.J. Polzin, J.G. Zhang, W. Xu, Electrolyte additive enabled fast charging and stable cycling lithium metal batteries, *Nat. Energy* 2 (2017) 17012.
- [3] C. Guo, Q.H. Wang, J.P. He, C.P. Wu, K.X. Xie, Y. Liu, W.C. Zhang, H.Y. Cheng, H. Hu, C. Wang, Rational design of unique ZnO/ZnS@N-C heterostructures for high performance lithium-ion batteries, *J. Phys. Chem. Lett.* 11 (2020) 905–912.
- [4] Q.X. Xie, Y.F. Zhang, D.L. Xie, P. Zhao, EDTA-Fe(III) sodium complex-derived bubble-like nitrogen-enriched highly graphitic carbon nanospheres as anodes with high specific capacity for lithium-ion batteries, *Ionics* 26 (2020) 85–94 (Kiel).
- [5] J.X. Li, Q.X. Xie, P. Zhao, C.P. Li, EDTA-Co(II) sodium complex derived Co(OH)<sub>2</sub>/Co<sub>3</sub>O<sub>4</sub>/Co nanoparticles embedded in nitrogen-enriched graphitic

- porous carbon as lithium-ion battery anode with superior cycling stability, *Appl. Surf. Sci.* 504 (2020) 144515.
- [6] M.V. Reddy, G.V. SubbaRao, B.V.R. Chowdari, Metal oxides and oxysalts as anode materials for Li ion batteries, *Chem. Rev.* 113 (2013) 5364–5457.
  - [7] M. Yang, Y. Hou, N.A. Kotov, Graphene-based multilayers: critical evaluation of materials assembly techniques, *Nano Today* 7 (2012) 430–447.
  - [8] J. Xiang, Z.P. Wu, X.K. Zhang, S.S. Yao, Enhanced electrochemical performance of an electrospun carbon/MoO<sub>2</sub> composite nanofiber membrane as self-standing anodes for lithium-ion batteries, *Mater. Res. Bull.* 100 (2018) 254–258.
  - [9] L.F. Shen, Q. Che, H.S. Li, X.G. Zhang, Mesoporous NiCo<sub>2</sub>O<sub>4</sub> nanowire arrays grown on carbon textiles as binder-free flexible electrodes for energy storage, *Adv. Funct. Mater.* 24 (2014) 2630–2637.
  - [10] S.H. Kang, D.P. Abraham, A. Xiao, B.L. Lucht, Investigating the solid electrolyte interphase using binder-free graphite electrodes, *J. Power Sources* 175 (2008) 526–532.
  - [11] X.H. Cao, Y.M. Shi, W.H. Shi, X.H. Rui, Q.Y. Yan, J. Kong, H. Zhang, Preparation of MoS<sub>2</sub>-coated three-dimensional graphene networks for high-performance anode material in lithium-ion batteries, *Small* 9 (2013) 3433–3438.
  - [12] J. Guo, H.L. Jiang, X.C. Li, Z. Chu, W.J. Zheng, Y. Dai, X.B. Jiang, X.M. Wu, G.H. He, Defective graphene coating-induced exposed interfaces on CoS nanosheets for high redox electrocatalysis in lithium-sulfur batteries, *Energy Storage Mater.* 40 (2021) 358–367.
  - [13] L.G. Guo, H. Sun, C.Q. Qin, W. Li, F. Wang, W.L. Song, J. Du, F. Zhong, Y. Ding, Flexible Fe<sub>3</sub>O<sub>4</sub> nanoparticles/N-doped carbon nanofibers hybrid film as binder-free anode materials for lithium-ion batteries, *Appl. Surf. Sci.* 459 (2018) 263–270.
  - [14] C.Y. Zhou, X.C. Li, H. Jiang, Y. Ding, G.H. He, J. Guo, Z. Chu, G.H. Yu, Pulverizing Fe<sub>2</sub>O<sub>3</sub> nanoparticles for developing Fe<sub>3</sub>C/N-codoped carbon nanoboxes with multiple polysulfide anchoring and converting activity in Li-S batteries, *Adv. Funct. Mater.* 31 (2021) 2011249.
  - [15] C. Guo, W.C. Zhang, Y. Liu, J.P. He, S. Yang, M.K. Liu, Q.H. Wang, Z.P. Guo, Constructing CoO/Co<sub>3</sub>S<sub>4</sub> heterostructures embedded in N-doped carbon frameworks for high-performance sodium-ion batteries, *Adv. Funct. Mater.* 29 (2019) 1901925.
  - [16] B. Wang, J. Cheng, Y. Wu, D. Wang, D. He, Electrochemical performance of carbon/Ni composite fibers from electrospinning as anode material for lithium ion batteries, *J. Mater. Chem. A* 1 (2013) 1368–1373.
  - [17] W.M. Zhang, X.L. Wu, J.S. Hu, Y.G. Guo, L.J. Wan, Carbon coated Fe<sub>3</sub>O<sub>4</sub> nanospindles as a superior anode material for lithium-ion batteries, *Adv. Funct. Mater.* 18 (2008) 3941–3946.
  - [18] D.W. Jung, J.H. Jeong, S.W. Han, E.S. Oh, Electrochemical performance of potassium-doped wüstite nanoparticles supported on graphene as an anode material for lithium ion batteries, *J. Power Sources* 315 (2016) 16–22.
  - [19] J.B. Mu, B. Chen, Z.C. Guo, M.Y. Zhang, Z.Y. Zhang, P. Zhang, C.L. Shao, Y.C. Liu, Highly dispersed Fe<sub>3</sub>O<sub>4</sub> nanosheets on one-dimensional carbon nanofibers: synthesis, formation mechanism, and electrochemical performance as supercapacitor electrode materials, *Nanoscale* 3 (2011) 5034.
  - [20] M.X. Gao, P. Zhou, P. Wang, J.H. Wang, C. Liang, J.L. Zhang, Y.F. Liu, FeO/C anode materials of high capacity and cycle stability for lithium-ion batteries synthesized by carbothermal reduction, *J. Alloy. Compd.* 565 (2013) 97–103.
  - [21] X.Y. Zhao, D.G. Xia, J.C. Yue, S.Z. Liu, *In-situ* generated nano-Fe<sub>3</sub>C embedded into nitrogen-doped carbon for high performance anode in lithium ion battery, *Electrochim. Acta* 116 (2014) 292–299.
  - [22] J.X. Li, W.W. Wen, G.G. Xu, M.Z. Zou, Z.G. Huang, L.H. Guan, Fe-added Fe<sub>3</sub>C carbon nanofibers as anode for Li ion batteries with excellent low-temperature performance, *Electrochim. Acta* 153 (2015) 300–305.
  - [23] Z.P. Zhou, C.L. Lai, L.F. Zhang, Y. Qian, H.Q. Hou, D.H. Reneker, H. Fong, Development of carbon nanofibers from aligned electrospun polyacrylonitrile nanofiber bundles and characterization of their microstructural, electrical, and mechanical properties, *Polymer* 50 (2009) 2999–3006 (Guildf).
  - [24] M.E. Im, D. Pham-Cong, J.Y. Kim, H.S. Choi, J.H. Kim, J.P. Kim, J. Kim, S.Y. Jeong, C.R. Cho, Enhanced electrochemical performance of template-free carbon-coated iron(II, III) oxide hollow nanofibers as anode material for lithium-ion batteries, *J. Power Sources* 284 (2015) 392–399.
  - [25] Q.X. Xie, Y.F. Zhang, D.L. Xie, P. Zhao, Nitrogen-enriched graphitic carbon encapsulated Fe<sub>3</sub>O<sub>4</sub>/Fe<sub>3</sub>C/Fe composite derived from EDTA-Fe(III) sodium complex as LIBs anodes with boosted performance, *J. Electroanal. Chem.* 857 (2020) 113749.
  - [26] T. Yamashita, P. Hayes, Analysis of XPS spectra of Fe<sup>2+</sup> and Fe<sup>3+</sup> ions in oxide materials, *Appl. Surf. Sci.* 254 (2008) 2441–2449.
  - [27] J.P. Hong, S.B. Lee, Y.W. Jung, J.H. Lee, K.S. Yoon, K.W. Kim, C.O. Kim, C.H. Lee, M.H. Jung, Room temperature formation of half-metallic Fe<sub>3</sub>O<sub>4</sub> thin films for the application of spintronic devices, *Appl. Phys. Lett.* 83 (2003) 1590–1592.
  - [28] D. Wilson, M.A. Langell, XPS analysis of oleylamine/oleic acid capped Fe<sub>3</sub>O<sub>4</sub> nanoparticles as a function of temperature, *Appl. Surf. Sci.* 303 (2014) 6–13.
  - [29] Y.G. Huang, X.L. Lin, X.H. Zhang, Q.C. Pan, Z.X. Yan, H.Q. Wang, J.J. Chen, Q.Y. Li, Fe<sub>3</sub>C@carbon nanocapsules/expanded graphite as anode materials for lithium ion batteries, *Electrochim. Acta* 178 (2015) 468–475.
  - [30] J.S. Li, S.L. Li, Y.J. Tang, M. Han, Z.H. Dai, J.C. Bao, Y.Q. Lan, Nitrogen-doped Fe/Fe<sub>3</sub>C@graphitic layer/carbon nanotube hybrids derived from MOFs: efficient bifunctional electrocatalysts for ORR and OER, *Chem. Commun.* 51 (2015) 2710–2713.
  - [31] B. Pal, M. Sharon, Preparation of iron oxide thin film by metal organic deposition from Fe(III)-acetylacetonate: a study of photocatalytic properties, *Thin Solid Films* 379 (2000) 83–88.
  - [32] B.H. Xu, L.B. Yu, X. Zhao, H.R. Wang, C. Wang, L.Y. Zhang, G.L. Wu, Simple and effective synthesis of zinc ferrite nanoparticle immobilized by reduced graphene oxide as anode for lithium-ion batteries, *J. Colloid Interf. Sci.* 584 (2021) 827–837.
  - [33] S.H. Chen, J.F. Wu, R.H. Zhou, L. Zuo, P. Li, Y.H. Song, L. Wang, Porous carbon spheres doped with Fe<sub>3</sub>C as an anode for high-rate lithium-ion batteries, *Electrochim. Acta* 180 (2015) 78–85.
  - [34] C. Guo, J.P. He, X.Y. Wu, Q.W. Huang, Q.P. Wang, X.S. Zhao, Q.H. Wang, Facile fabrication of honeycomb-like carbon network-encapsulated Fe/Fe<sub>3</sub>C/Fe<sub>3</sub>O<sub>4</sub> with enhanced Li-storage performance, *ACS Appl. Mater. Inter.* 10 (2018) 35994–36001.
  - [35] H.L. Lyu, J.R. Liu, S. Qiu, Y.H. Cao, C.X. Hu, S.M. Guo, Z.H. Guo, Carbon composite spun fibers with *in situ* formed multicomponent nanoparticles for a lithium-ion battery anode with enhanced performance, *J. Mater. Chem. A* 4 (2016) 9881–9889.
  - [36] M.Z. Zou, L.L. Wang, J.X. Li, L.H. Guan, Z.G. Huang, Enhanced Li-ion battery performances of yolk-shell Fe<sub>3</sub>O<sub>4</sub>@C anodes with Fe<sub>3</sub>C catalyst, *Electrochim. Acta* 233 (2017) 85–91.
  - [37] R. Yang, Y.M. Wang, Q.J. Deng, P. Hui, Z.B. Luo, Y.L. Yan, L.L. Wang, Metal-organic framework derived Fe<sub>3</sub>O<sub>4</sub>/C/rGO composite as an anode material in lithium-ion batteries, *Ionics* 27 (2021) 3281–3289 (Kiel).
  - [38] Y. Liu, X.Y. Li, A.K. Haridas, Y.Z. Sun, J. Heo, J.H. Ahn, Y. Lee, Biomass-derived graphitic carbon encapsulated Fe/Fe<sub>3</sub>C composite as an anode material for high-performance lithium ion batteries, *Energies* 13 (2020) 827.
  - [39] A.Y. Shenouda, H.K. Liu, Electrochemical behaviour of tin borophosphate negative electrodes for energy storage systems, *J. Power Sources* 185 (2008) 1386–1391.
  - [40] M. Sun, Z.P. Cui, H.Q. Liu, S.J. Li, Q.Y. Zhang, X.L. Sheng, Y.Q. Wang, Graphene-wrapped FeOOH nanorods with enhanced performance as lithium-ion battery anode, *Nano* 16 (2020) 2150005.
  - [41] X.C. Li, Y. Zhang, S.T. Wang, Y. Liu, Y. Ding, G.H. He, X.B. Jiang, W. Xiao, G.H. Yu, Scalable high-areal-capacity Li-S batteries enabled by sandwich structured hierarchically porous membranes with intrinsic polysulfide adsorption, *Nano Lett.* 20 (2020) 6922–6929.
  - [42] Z.P. Cui, M. Sun, H.Q. Liu, S.J. Li, Q.Y. Zhang, C.P. Yang, G.J. Liu, J.Y. Zhong, Y.Q. Wang, Double-shell SnO<sub>2</sub>@Fe<sub>2</sub>O<sub>3</sub> hollow spheres as a high-performance anode material for lithium-ion batteries, *CrystEngComm* 22 (2020) 1197–1208.
  - [43] Y.K. Tang, L. Liu, H.T. Zhao, Y. Zhang, L.B. Kong, S.S. Gao, X.H. Li, L. Wang, D.Z. Jia, Pseudocapacitive behaviors of Li<sub>2</sub>FeTiO<sub>4</sub>/C hybrid porous nanotubes for novel lithium-ion battery anodes with superior performances, *ACS Appl. Mater. Inter.* 10 (2018) 20225–20230.